Microstructure and mechanical behaviour of a Nextel™610/alumina weak matrix composite subjected to tensile and compressive loadings

Camélia Ben Ramdane, Aurélie Julian-Jankowiak, Roger Valle, Yves Renollet, Michel Parlier, Éric Martin, Pascal Diss

Microstructure and mechanical behaviour of a Nextel^{TM}610/alumina weak matrix composite subjected to tensile and compressive loadings

C. Ben Ramdane[a,b,c], A. Julian-Jankowiak[b,*], R. Valle[b], Y. Renollet[b], M. Parlier[b], E. Martin[d], P. Diss[a]

[a] *Herakles, Rue de Touban, Les cinq chemins, F-33185 Le Haillan, France*
[b] *ONERA-The French Aerospace Lab, 29 avenue de la Division Leclerc, F-92322 Châtillon, France*
[c] *Université de Bordeaux, 351 Cours de la Libération, F-33400 Talence, France*
[d] *Laboratoire des Composites Thermo-Structuraux, CNRS UMR 5801, Université de Bordeaux, 3 rue de La Boétie, F-33600 Pessac, France*

The present study was aimed at determining the mechanical behaviour of a weak matrix oxide/oxide CMC subjected to tensile and compressive loadings in the fibre direction and at identifying the damage mechanisms. The material consisted of Nextel^{TM}610 fibres (8 HSW) embedded in an alumina matrix, with a 49 % fibre volume fraction and 24 ± 2 % total porosity. The average ultimate tensile stress and strain of the material were, respectively, 260 ± 37 MPa and 0.3 ± 0.09 % under tensile loading and −261 ± 69 MPa and−0.19 ± 0.04 % under compressive loading. Three types of pores were differentiated within the material: nanopores (13 ± 1 %), micropores (6 ± 2 %) and macropores (5 ± 1 %). The latter appear to be the most detrimental for the material, enhancing delamination. The damage mechanisms of the material were assessed through SEM examination and *in situ* tensile tests.

1. Introduction

Two solutions have emerged to reduce aircraft greenhouse gases emissions: lightening the aircrafts and increasing the operating temperature of the gas turbines and, as a consequence, of the exhaust gases. Composite materials have been widely used during the last decades to reduce weight. Ceramic matrix composites (CMCs), used for thermostructural applications [1], fulfil both requirements: their density is lower than that of conventional nickel-based superalloys and they are capable of maintaining excellent strength and fracture toughness at high temperatures [2–5]. Moreover, these materials, designed for applications in oxidizing environments (turbo-engines), have to be oxidation-resistant and thermodynamically stable [2]. Non-oxide CMCs, generally SiC/SiC composites, show poor oxidation resistance at intermediate temperatures lower than 700–800 °C [3]. Therefore, oxide fibre/oxide matrix CMCs appear to be good candidates for thermostructural applications in this temperature range [6]. Despite their better oxidation resistance compared to SiC/SiC composites in the considered temperature range, oxide/oxide composites exhibit lower mechanical properties and cannot be used at temperatures higher than 1000–1100 °C for long duration applications. Beyond these temperatures, fibre degradation [7] induces a decrease in mechanical properties [8].

It is now commonly assumed that the mechanical performance of CMCs relies on the fibre/matrix interface. When matrix cracks initiate and propagate under loading, it seems necessary to isolate the fibres from the matrix so that they remain intact and ensure the mechanical strength of the composite [9]. Therefore, two approaches exist: weak matrix and weak interface composites [9–11]. The weak matrix approach is based on a porous matrix. In these composites, cracks propagate between the grains of the porous matrix, which enables energy dissipation, and, when matrix cracks reach the fibres, they are deflected at the fibre/matrix interface. This leads to fibre/matrix debonding and fibre pull-out, thereby providing high composite toughness [8,12]. The weak matrix concept assumes a strong fibre/matrix bond, but the high porosity of the matrix, even at the fibre/matrix interface, ensures a weak fibre/matrix interface.

Regarding the second approach, it is based on a weak fibre/matrix interface promoting fibre/matrix debonding and sliding. This can be achieved by introducing a weak interphase between the fibres and the matrix, which is generally fully dense. Such an

* Corresponding author.
E-mail address: aurelie.jankowiak@onera.fr (A. Julian-Jankowiak).

interphase consists of a fibre coating, which increases the process cost [12].

Thus, the weak matrix approach appears to be very attractive. According to previous studies, the matrix porosity must be in the 30–40% range to obtain a weak matrix composite [1,8,13]. Regarding the fibre volume fraction, it is essential, for turbo-engine applications, to manufacture materials with a high fibre volume fraction in order to enhance the mechanical properties of the composite material, especially the Young's modulus. Hence, the aimed fibre volume fraction and total porosity were 50% [14] and 25%, respectively.

Most of the oxide/oxide composites described in previous studies were reinforced with commercial Nextel^{TM}610 or Nextel^{TM}720 fibres embedded in an alumina, an alumina-silica or an alumina-mullite matrix. Nextel^{TM}610 alumina fibres offer high strength [12] at low and moderately high temperatures (up to approximately 1000 °C) whereas Nextel^{TM}720 alumina-silica fibres have good creep resistance up to approximately 1200 °C [8]. As for the matrix, the main advantage of alumina is that its sintering process can start at temperatures lower than 1000–1100 °C. Beyond this temperature range, a loss of mechanical properties of Nextel^{TM}610 fibres occurs. Thus, combining Nextel^{TM}610 alumina fibres with an alumina matrix offers two advantages: (i) the matrix can be partially sintered without damaging the fibres and (ii) there is no reaction (except sintering) between fibres and matrix, thus allowing crack deflection in this interface and, consequently, fibre/matrix debonding.

The objective of this study is to investigate the microstructure and the mechanical behaviour of a weak matrix alumina/alumina composite under tensile and compressive loadings at room temperature and to identify the damage mechanisms of this composite [15] in order to assess the relationships between the microstructure, resulting from the manufacturing process, and the damage mechanisms. A deep understanding of these relationships, mandatory to improve the mechanical properties of the materials, seems to be absent from the literature. Several techniques were used to establish a correlation between microstructure, mechanical behaviour and damage mechanisms: porosimetry, X-ray computed microtomography (μCT), scanning electron microscope (SEM) examinations and *in situ* tensile testing in SEM.

Finally, the discussion will be essentially focused on the specific role of the identified damage mechanisms leading to failure of the Nextel^{TM}610/alumina weak matrix composite subjected to either tensile or compressive loadings [15].

2. Experimental procedure

2.1. Material

The material consisted of woven Nextel^{TM}610 alumina fibres, without coating, embedded in a porous alumina matrix. The woven fabric was an 8 harness satin weave. After desizing in air at 700 °C, the fibre reinforcement was infiltrated (paint brush deposition) with a water-based alumina matrix slurry, then dried and cut into twelve plies. A lay-up process was then used to manufacture the Nextel^{TM}610/alumina plates: the prepregs were infiltrated with water, laid up in a mould and hot pressed at 100 °C and low pressure (<1 MPa) in a vacuum bag. Finally, the plates were heat treated at 1200 °C for a few minutes (pressureless sintering) to obtain approximately 2.5 mm thick plates with the required porosity and fibre volume fraction.

Quality of each manufactured composite plate was checked using infrared thermography. This technique allows excluding the plates where large delamination areas are detected.

Moreover, in order to evaluate the thermomechanical properties of the matrix, neat matrix specimens were uniaxially cold-pressed (20–40 MPa) and sintered at different temperatures to reach different porosity levels (10, 20, 25 and 38 %).

2.2. Mechanical testing and damage monitoring

The ultimate tensile strength of the neat matrix was determined through 4-point bending tests on 35 x 5 x 1.8 mm^3 specimens with a constant displacement rate of 0.3 mm.min^{-1}. The Young's modulus was measured on the same samples through a dynamic resonance method (Impulse Excitation Technique) using a GrindoSonic Mk5i testing instrument.

In-plane mechanical properties of the Nextel^{TM}610/alumina composite were studied through uniaxial monotonic tensile and compressive loadings in the fibre direction (weft direction). All tests were conducted at room temperature in laboratory air environment, using a servocontrolled Z150 Zwick/Roell Materials testing machine. The tests were performed in stroke control with a constant displacement rate of 0.5 mm.min^{-1}.

Straight-sided specimens, 16 mm x 150 mm *x composite thickness* (tensile tests) or 30 mm x 120 mm *x composite thickness* (compression tests), with a gauge length of 70 mm (tensile tests) or 30 mm (compression tests) were used [15]. For both tensile and compression tests, pure aluminium annealed thin foils (0.2 mm thick) are used as tabs to ensure load transfer to the specimen, without damage.

Strain measurements were performed using simultaneously digital image correlation (DIC, VIC-3D^{TM}), uniaxial extensometry (Schenck, 25 mm gauge length) and strain gauges (Vishay Precision Group, CEA-06-250UW-350). After test result analysis, it appeared that the uniaxial extensometer slid on the surface of the specimens. Besides, the strains measured by DIC and by strain gauges were very similar. Thus, only the strains measured by DIC were taken into account.

Young's moduli were determined graphically from stress-strain curves and damage thresholds were defined as the stress and strain corresponding to the elastic limit (yield point), for each tested specimen.

In order to provide information concerning the evolution of damage occurring under different loading levels, interrupted tensile tests have been performed, the maximum stress being equal to 22, 59, 63 and 85 % of the average tensile failure strength. The corresponding damage mechanisms were then investigated through microscope examination of longitudinal cross-sections of these specimens.

Real-time monitoring of some monotonic tensile and compressive tests was ensured through acoustic emission (AE) using 8 mm in diameter sensors (Nano30, Physical Acoustic Corp., NJ, USA).

For cyclic loading tests, the specimens were sequentially loaded at different stresses, with a return to zero load between two cycles. The sequential stresses were determined from monotonic tensile tests and correspond to different points on the stress-strain curves: a point slightly after the average damage threshold, a point just before the average failure and intermediate points. The stresses levels were thus: 23 %, 42 %, 58 %, 74 %, 86 % and 98 % of the average ultimate tensile strength of the material (*i.e.* 60 MPa, 110 MPa, 150 MPa, 192 MPa, 225 MPa and 250 MPa). Three specimens, cut from three different plates, were used to perform these tests.

The interlaminar shear strength (ILSS) of the composite was measured through 3-point bending tests on short beams according to BS EN 658:5-2002 Standard, in the fibre (weft) direction. The dimensions of ILSS test specimens were 25 mm × 10 mm × *composite thickness*. The cylindrical rollers had a diameter of 4 mm and the outer support span was 15 mm. A dis-

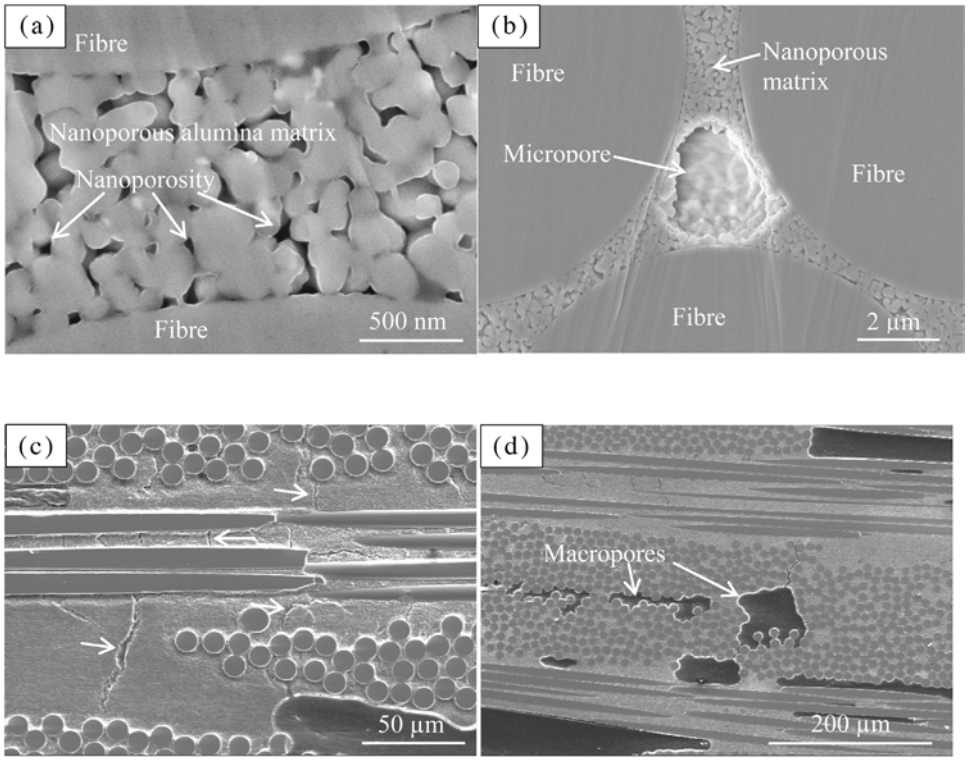

Fig. 1. SEM observations of as-processed Nextel^{TM}610/alumina composite. (a) Nanoporosity of the matrix (ion polishing), enabling crack deflection at the fibre/matrix interface. (b) Micropore between three fibres (ion polishing). (c) Sintering shrinkage matrix cracks, perpendicular to the plies. (d) Intraply macropores, due to a lack of matrix, and crack initiation at macropores.

placement rate of 0.5 mm min^{-1} was used for these tests. The ILSS (MPa) was calculated using the following equation

$$\mathrm{ILSS} = \frac{3\,\mathrm{F}}{4\,\mathrm{b}\,\mathrm{h}} \tag{1}$$

where F is the shear failure force (N), b is the mean test specimen width (mm) and h is the mean test specimen thickness (mm).

2.3. Microstructural characterization

Total porosity and pore size distribution of the as-processed composite were measured by Archimedes' method in water and mercury intrusion porosimetry, respectively. More than six samples from six different plates were considered. Mercury porosimetry was performed at ISM (Institut des Sciences Moléculaires, University of Bordeaux, France), using a Micromeritics Autopore IV 9500 porosimeter. The total porosity results obtained by these two techniques were similar.

Spatial distribution of pores was also studied through 3D computed tomography analysis. A Phoenix v|tome|x L300 (General Electric Sensing and Inspection Technologies) X-ray tomograph was used for data acquisition, with a 180 kV source, enabling a 10.2 µm resolution (voxel size). The scanned zone of the samples was approximately 21 mm × 16 mm × *composite thickness*. The advantage of this technique, as compared to the porosimetry techniques, is that it allows determination of the size and of the spatial distribution of pores larger than the voxel size. A watershed segmentation method, coupled with a k-means method, was used to calculate the porosity in each layer of the Zone Of Interest (ZOI), 9.2 mm × 9.2 mm × *composite thickness* in size.

In order to identify the damage mechanisms of the composites under tensile loading, SEM examinations (Zeiss DSM-962 and Zeiss Gemini FEG-SEM) were performed on as-processed and damaged composites (*post-mortem* observations) [15]. The observation of as-processed materials and damaged specimens required a specific preparation. First, they were impregnated by an epoxy resin (in a vacuum chamber for a good porosity impregnation), in order to *(i)* avoid further damaging of the samples during polishing and *(ii)* have a flat polished surface, the fibres and the matrix being equally polished. Then, the samples were cut in the middle planes, parallel and perpendicular to the loading direction (parallel and perpendicular to the weft direction in the case of as-processed material). Finally, the obtained cross-sections were mirror polished for SEM examination.

In situ tensile tests were carried out in SEM (*Zeiss DSM-960*) in order to: *(i)* corroborate the *post mortem* observations and *(ii)* ascertain the chronology of the damage mechanisms. *In situ* testing offers two advantages: real time damage monitoring and observation of the material under load, which prevents crack closure when returning to zero load. This phenomenon cannot be avoided in the case of *post mortem* observation. But *in situ* testing also has disadvantages. First of all, the technique requires the use of small straight sided specimens (3 mm x 40 mm x *composite thickness*) with a 10 mm gauge length, whereas the geometrical unit cell of the composite attains 8 mm x 8 mm x *composite thickness*. Moreover, the observation of damage being performed on the specimen edge, the observed mechanisms are thus occurring in a plane stress state. The observed edge of the specimens was mirror polished prior to testing (without resin impregnation). The samples were observed in real-time during loading tests and images of the total gauge length were acquired after each 100 N loading step (approximately 13 MPa considering the section of the specimens), while the specimens were maintained under constant load.

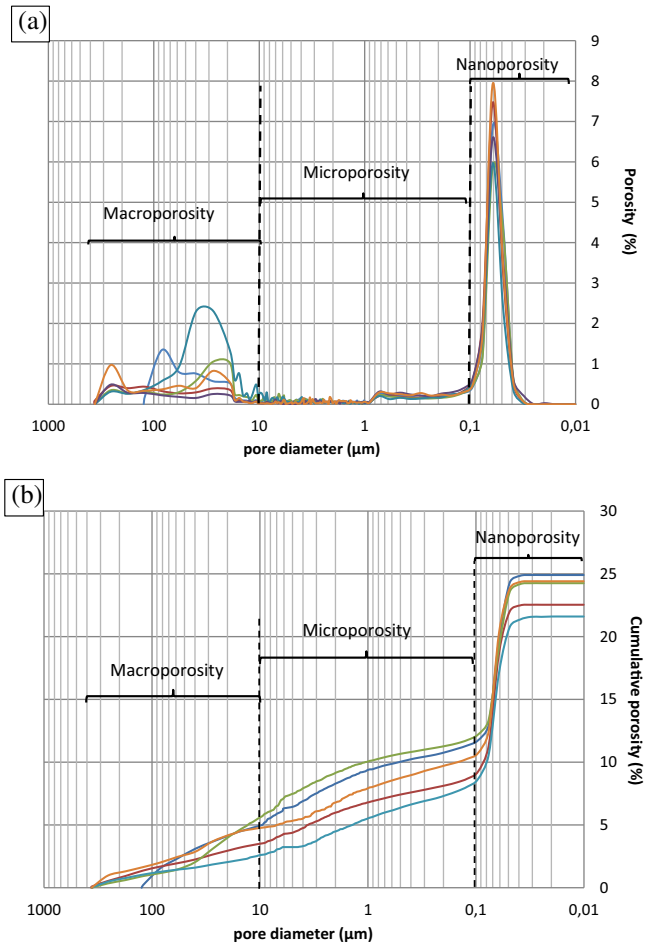

Fig. 2. Pore size distribution as determined by mercury intrusion porosimetry. (a) Porosity vs. pore diameter. (b) Cumulative porosity vs. pore diameter.

3. Results and discussion

3.1. Microstructure

The total open porosity, determined by Archimedes' method, was 24 ± 2 % and the fibre volume fraction thus deduced was 49 %. Several types of pores were detected through mercury intrusion porosimetry and SEM examinations (Figs. 1 and 2):

- Nanopores, only located in the matrix (Fig. 1a),
- Micropores, corresponding to pores and also microcracks (Fig. 1b and c),
- Macropores, located between plies (interply macropore) or inside a ply (intraply macropore) (Fig. 1d).

Quantification of each type of pore was performed through coupling of the various porosity measurement methods. Nanopores are considered as pores smaller than 0.1 µm in diameter and macropores as pores larger than 10 µm as regards to mercury intrusion (Fig. 2). Thus, the nanoporosity was 13 ± 1 % (volume fraction) of the composite and represented a volume fraction of 32 ± 1 % of the matrix. This fraction stands within the 30–40 % porosity range required for a weak matrix. In this respect, the UTS and the Young's modulus of the 32 % porosity neat matrix were determined through exponential fits from the values corresponding to specimens with 10, 20, 25 and 38 % porosity. The UTS and the Young's modulus were estimated respectively at 45 MPa and 80 GPa (Table 1). Even if only approximate, these values allow characterising the mechanical behaviour of the neat matrix.

Table 1
Mechanical properties of N610 fibres (supplier's data) and of the neat alumina 32% porosity matrix at room temperature.

	UTS (MPa)	E (GPa)
N610 fibre	2930	373
Al_2O_3 32% porosity matrix	≈45	≈80

Table 2
Porosity and fibre volume fraction as determined by mercury intrusion porosimetry (five samples from five different plates).

Total porosity (%)	24 ± 2
Fibre volume fraction (%)	49 ± 0
Macroporosity (%)	5 ± 1
Microporosity (%)	6 ± 2
Nanoporosity (%)	13 ± 1

The macroporosity is due to a lack of matrix (Fig. 1d) and represents 5 ± 1 % (volume fraction) of the composite (Fig. 2). The presence of large pores in oxide/oxide CMCs was reported in other studies [16] but not quantified. Two categories of macropores were identified: intraply and interply macropores. This distinction was assessed by means of X-ray tomography analysis and SEM observations, performed on as-processed materials (Figs. 1 and 3). Approximately 65 % of the macroporosity, measured by analysis of X-ray tomography data, consisted in interply macropores.

Microporosity, between 0.1 and 10 µm, represents 6 ± 2 % (volume fraction) of the composite. Pores, but also sintering shrinkage cracks are considered as micropores. Indeed, it should be noted that, even if fibres and matrix exhibit the same coefficients of thermal expansion, thus avoiding internal thermal stress after cooling, the matrix sintering shrinkage should be taken into account. Measurements performed on the neat matrix and on the thickness of the composite at 1200 °C have shown that shrinkage strain ($\Delta L/L_0$) attains 4.7%, whereas on the composite, in the fibre direction, it attains only 2.7%. Due to the absence of fibre shrinkage during matrix sintering, the only possibility to accommodate the matrix tensile stress resulting from sintering shrinkage is to slightly increase the undulation of the tows and, more essentially, to nucleate microcracks in the matrix of the as-processed material (see Fig. 1c). These cracks are predominantly normal to the direction of the woven reinforcement and concentrated in the matrix-rich regions. The presence of sintering shrinkage cracks is common in oxide/oxide composites and has been reported in several studies [1,3,8–10,17].

Finally, fibre volume fraction and porosity data measured on the studied material are summarized in Table 2.

3.2. Mechanical properties

3.2.1. Interlaminar shear strength

The interlaminar shear strength of the composite, measured by 3-point bending tests, is 20 ± 2 MPa. This value is higher than those reported by Simon [16] for Nextel™610/mullite composites (12.5–14 MPa) and Nextel™720/mullite composites (10–11.5 MPa). The material developed at ONERA is thus expected to be more resistant to delamination than the composites described in the literature with lower interlaminar shear strengths.

3.2.2. Tensile and compressive properties in the fibre direction

The tensile and compressive stress-strain curves are presented in Fig. 4. Average ultimate tensile strength and strain of the composite are 260 ± 37 MPa and 0.30 ± 0.09 %, with a Young's modulus of 134 ± 19 GPa (Table 3). The response of the composite, under

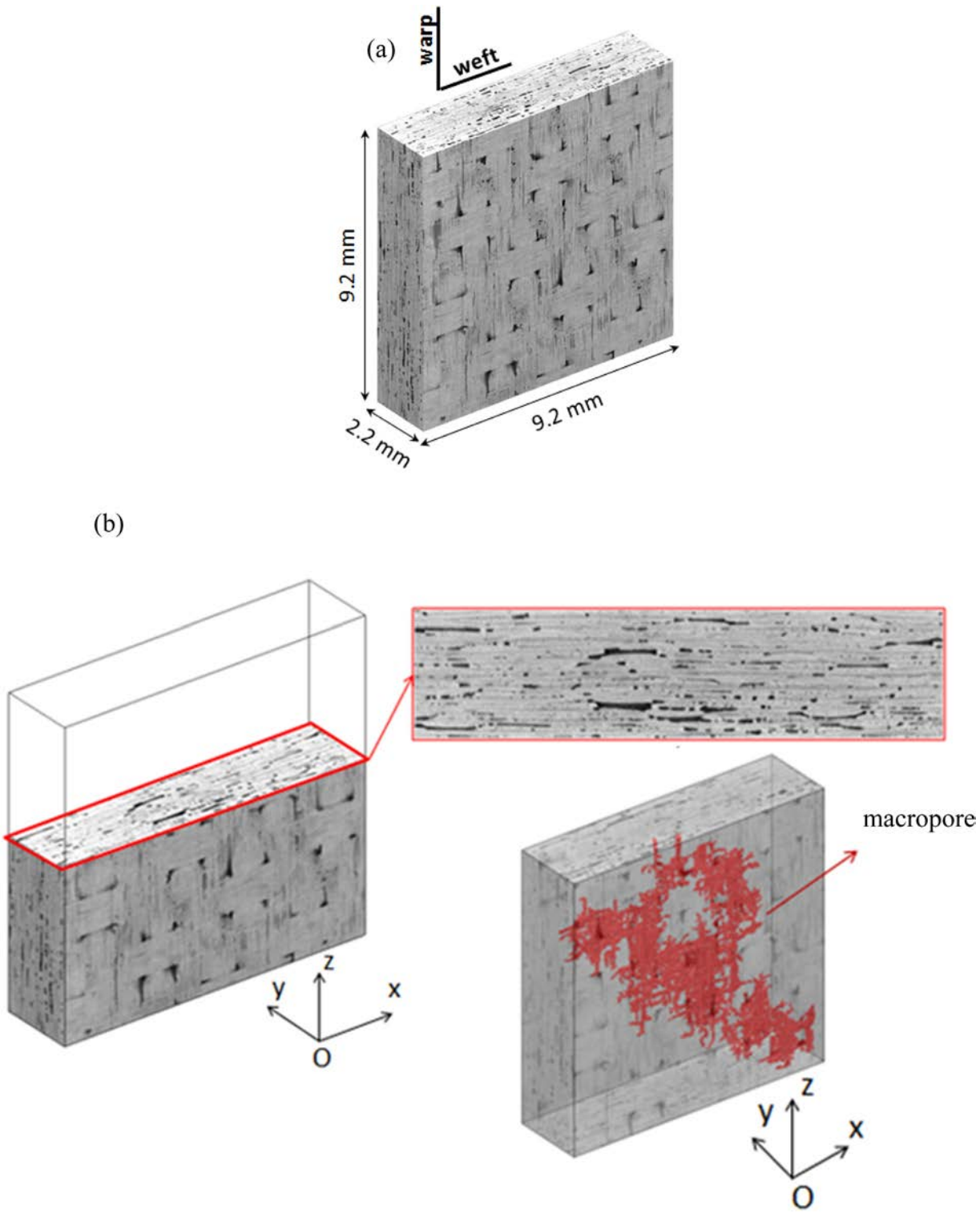

Fig. 3. X-Ray tomography analysis of Nextel^{TM}610/alumina composite. (a) Reconstruction of the zone of interest. (b) Macropores detected in each layer and example of a large macropore in the zone of interest.

Table 3
Mechanical properties of N610/alumina composite under tensile and compressive loadings at room temperature.

	σ (MPa)	ε (%)	$\sigma_{\text{Damage threshold}}$ (MPa)	$\varepsilon_{\text{Damage threshold}}$ (%)	E (GPa)
Tensile loading	260 ± 37	0.30 ± 0.09	48 ± 8	0.04 ± 0.01	134 ± 19
Compressive loading	-291 ± 69	-0.19 ± 0.04	-123 ± 31	-0.08 ± 0.02	161 ± 11

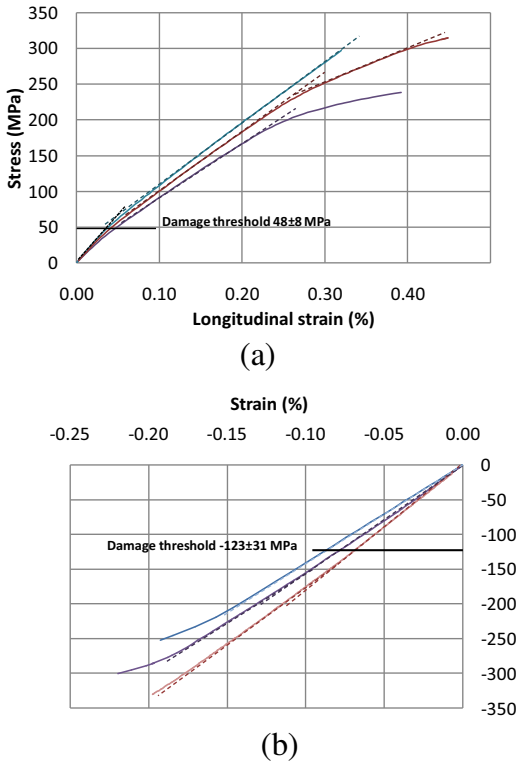

Fig. 4. Stress-strain curves of Nextel^{TM}610/alumina composite under tensile (a) and compressive (b) loadings in the fibre (weft) direction: distinction between the different domains of the curves, namely the elastic region (first linear part), the second quasi-linear part and, in some cases, the third part (generally non-linear). The damage threshold is determined as the end of the elastic region.

monotonic tensile loading in the fibre direction, shows a first linear segment, a second quasi-linear segment and, in some cases, a third non-linear segment (Fig. 4a). The first linear segment constitutes the elastic region of the material. In most cases, the failure occurs at the end of the second quasi-linear segment. Such a behaviour, described as nearly linear up to failure, is common in oxide/oxide composites and has been reported by several authors [5,8,17,18]. However, in these studies, the slope of the second segment is slightly lower than the Young's modulus whereas, in the present case, the slopes of the first two segments are clearly different, as shown in Fig. 4a.

Average ultimate compressive strength and strain of the composite are -291 ± 69 MPa and -0.19 ± 0.04 % with a Young's modulus of 161 ± 11 GPa (Table 3). The stress-strain curves exhibit first a linear segment and end with a non-linear segment. In some cases, a second quasi-linear segment is present between these two parts of the curves (Fig. 4b). As for tensile tests, the first linear segment constitutes the elastic region of the material. In all cases, failure occurs at the end of the last non-linear segment, the non-linearity indicating a substantial damage increase. The same behaviour can be observed on the compression curves of Nextel^{TM}610/monazite/alumina (*i.e.* with a monazite fibre coating) reported by Jackson et al. [2]. The Nextel^{TM}610/alumina composite under investigation is much stiffer than the composite with monazite coating studied by Jackson et al. [2]. This latter composite exhibits a lower strength of -113 MPa (*vs.* -291 ± 69 MPa) for an equivalent failure strain of -0.19 % (*vs.* -0.19 ± 0.04 %), with a Young's modulus of 74 GPa (*vs.* 161 ± 11 GPa). This can be partially attributed to the lower fibre volume fraction of the Nextel^{TM}610/monazite/alumina composite (30 %).

Young's modulus and maximum stress and strain of the studied composite are also higher than those of all-oxide composites, reinforced with Nextel^{TM}610 fibres and with similar fibre volume fractions, reported in the literature [16,17,19]. However, the comparison is difficult since the several all-oxide CMCs described do not exhibit the same porosity and fibre volume fraction and were produced by different processes.

The comparison between the mechanical behaviour of the Nextel^{TM}610/alumina composite under tensile and compressive loadings shows that the material is stiffer in the second case, showing higher modulus (Table 3). This can be essentially attributed to the compaction of the microporous matrix and macropore closure, when the composite is subjected to compressive loading, thus increasing the composite stiffness. In this context, it should be noted that a rough estimate of the composite Young's modulus (Appendix A), taking into account the presence of the transverse tows, ≈164 GPa, is closer to the value experimentally determined under compressive loading (161 ± 11 GPa) than to that determined under tensile loading (134 ± 19 GPa). Under compressive loading, closure of the sintering shrinkage cracks leads to a continuous matrix, thus fulfilling the calculation hypothesis. The composite Young's modulus, increased as compared to the situation of opened cracks under tensile loading, attains the calculated value.

The damage threshold, which is generally not reported in the literature, is essential in order to compare different materials and to design thermostructural parts. In the present case, the curved parts of the tensile and compressive curves, between the elastic region and the second quasi-linear segment, indicate a sudden damage increase and can be considered as the damage thresholds. The stress and strain at the damage threshold deduced from the tensile curves are 48 ± 8 MPa and 0.04 ± 0.01 % (Fig. 4a) and -123 ± 31 MPa and -0.08 ± 0.02 % from the compressive curves (Fig. 4b) (Table 3).

Under tensile loading, the damage threshold is markedly lower than under compressive loading (absolute value). The tensile value corresponds to a matrix stress of approximately 27 MPa with the rough assumption of continuous and linear elastic media (Appendix B). This value is lower than the estimated UTS of the neat matrix (45 MPa, Table 1) and the difference (≈18 MPa) can be attributed to tensile residual stresses resulting from matrix sintering shrinkage, to the calculation assumptions and to the absence of macropores and flaws in the neat matrix specimens. In fact, this rather small difference clearly suggests that these tensile residual stresses in the matrix would be released due to the formation of matrix microcracks and to an increase in the undulation amplitude of the tows. Otherwise, the tensile residual stresses in the matrix would be much higher and the damage threshold much lower. Under compressive loading, the damage threshold is much higher (absolute value) than under tensile loading. This difference can have several origins. First of all, closure of the matrix sintering shrinkage microcracks already necessitates a non-negligible compressive loading level. Secondly, the matrix is subjected to tensile residual stresses resulting from matrix sintering shrinkage; this stress component, opposite to the compressive loading, increases the damage threshold level.

Considering the hysteresis loops of the composite under cyclic tensile loading (Fig. 5), it should be noted that a marked increase in the residual strain is observed after loading from 60 MPa to 110 MPa and also after loading from 225 MPa to 250 MPa. Damage thus seems to be essentially concentrated in these two regions corresponding to the curved portions of the tensile curve (Fig. 4) located between the linear and quasi-linear segments and between this quasi-linear segment and the last quasi-linear segment.

Typical tensile and compressive stress–strain curves, with corresponding acoustic emission signals (AE counts and cumulative energy) are reported in Fig. 6a and b, respectively. In both cases, if the loading amplitude is smaller than the damage thresholds (48 ± 8 MPa and -123 ± 31 MPa, respectively), the acoustic emis-

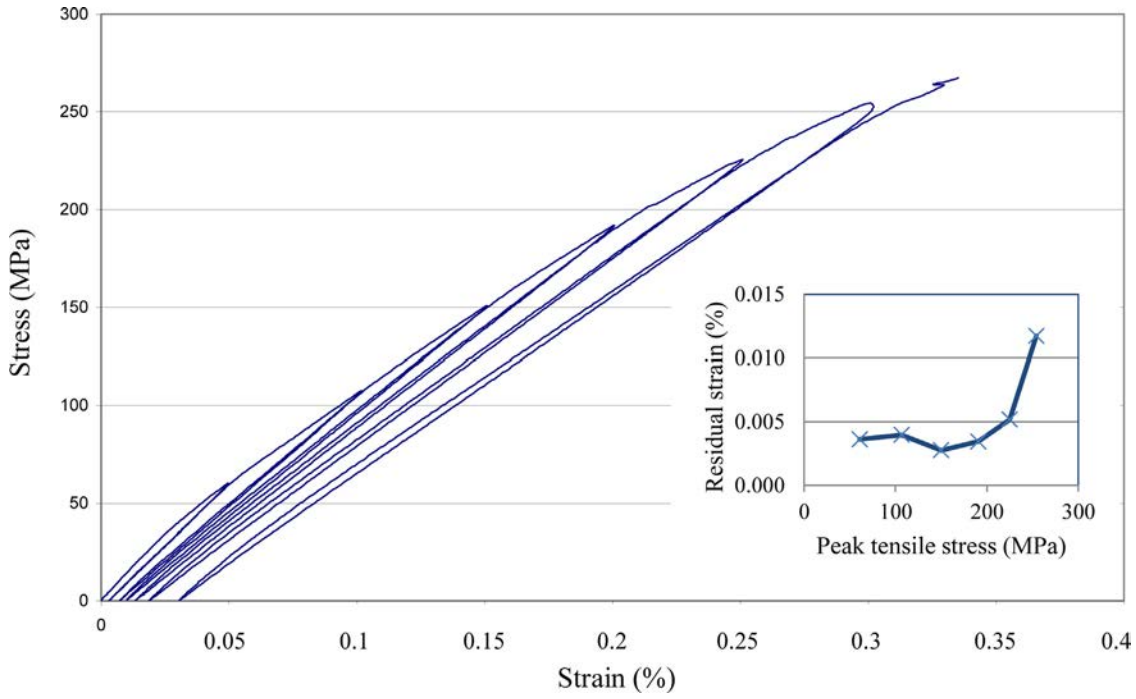

Fig. 5. Tensile stress/strain hysteresis loops of Nextel^{TM}610/alumina composite under cyclic tensile loading in the fibre (weft) direction. (inset: residual strain *vs.* peak tensile stress).

sion activity is negligible. Under tensile loading, the quasi-linear segment corresponds to a small and regular activity (AE counts and cumulative energy). At the end of the quasi-linear segment, the acoustic emission activity increases drastically, due, most probably, to fibre failures, finally leading to the composite failure. Under compressive loading, a more intense but rather less regular AE activity is detected, not only during the quasi-linear segment, but also during the end of the test, up to final failure.

The mechanical properties of the material are summarized in Table 3. As expected considering the heterogeneous microstructure of the material, the mechanical properties of the composite are slightly scattered; nevertheless, all the tensile and compressive curves (Fig. 4) exhibit, respectively, the same shape. Then, a study of the damage mechanisms and of their chronology is proposed to understand the role of the microstructure.

3.3. *Identification of the damage mechanisms*

As aforementioned, the damage mechanisms of the material were studied through *post mortem* SEM observations and *in situ* SEM tensile testing in order to suggest a damage scenario of the composite under tensile and compressive loadings.

Optical micrographs of fracture surfaces of the composite, tensile or compressive tested under monotonic loadings are presented in Fig. 7. In both cases, fibre pull-out and delamination are observed, the damage zones attaining ≈20 mm in length. However, under compressive loading, the side view (Fig. 7d) reveals a "brushy" appearance, consisting in a widely opened structure of delaminated plies, debonded tows and fibres. These observations of fracture surfaces thus already suggest a difference in the damage mechanisms leading to failure under tensile or compressive loadings.

Interrupted tensile tests have been performed at 58, 154, 165 and 220 MPa. SEM examination of longitudinal cross-sections of these specimens has provided information regarding the occurrence of the damage mechanisms. No damage can be observed below 165 MPa. Then, new inter-yarn matrix cracks, perpendicular to the loading direction are observed in the specimen tensile tested under 165 MPa (Fig. 8a). However, these cracks do not propagate along the longitudinal tows. Furthermore, at this stress level, macropores do not seem to be related to crack nucleation and propagation. Under 220 MPa loading, inter-yarn matrix cracks, also perpendicular to the loading direction, are more numerous and propagate through the transverse tows. Moreover, nucleation and propagation of cracks from the macropores are observed (Fig. 8b). Then, after failure (Fig. 8c and d), matrix crack initiation at the macropores and matrix crack deflection in the fibre/matrix interface can be observed. These cracks propagate along the longitudinal and transverse tows.

Fracture surface examination shows that fibre failure events are uncorrelated, the distance between the fracture surfaces of different fibres belonging to the same tow attaining a few hundred micrometers (Fig. 8e and f). This asserts the fact that the weak matrix allows separating the fibres from each other by fibre/matrix debonding within the tows. Levi et al. [1], Zok et al. [8] and Simon [16] reported the same phenomenon for other weak matrix oxide/oxide composites. According to Kostopoulos et al. [20] who identified the failure mechanisms in oxide/oxide composites using acoustic emission, matrix cracking occurs all along loading with an abrupt increase at a certain critical load.

A more precise chronology of such damage mechanisms has been established using *in situ* tensile tests. In this respect, transverse crack nucleation in matrix rich areas seems to appear first under ≈ 63–112 MPa and then an increase in crack formation appears from 192 MPa, up to 289 MPa (Fig. 9a to d). Moreover, the *in situ* tensile testing has allowed the observation of a crack, nucleated in a transverse tow, falling into a macropore (Fig. 9e and f). Macropores can thus be also considered as sinks for, at least, short and localized cracks. Such a mechanism can explain, at least partially, the rather good mechanical behaviour of the composite, in spite of the presence of macropores.

SEM observations of Nextel^{TM}610/alumina composites subjected to compressive loading have evidenced specific damage mechanisms leading to failure. For example, a matrix crack, nucleated on the edge of a macropore in a direction parallel to the loading

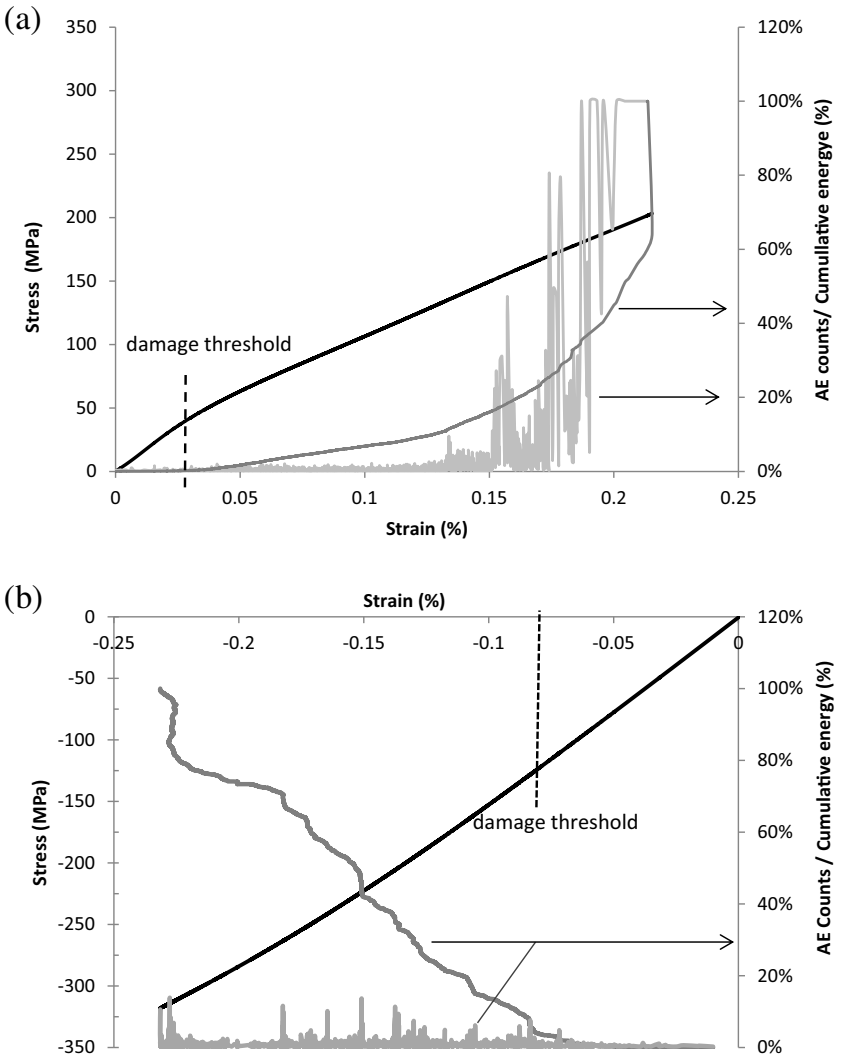

Fig. 6. AE counts, cumulative energy and stress-strain curves of Nextel^{TM}610/alumina composite under tensile (a) and compressive (b) loadings in the fibre (weft) direction. For the sake of comparison, the same scales are used for AE counts and cumulative energy for both tensile and compressive tests.

axis, is deflected in a direction oriented at $\approx 45^{\circ}$ to the loading axis and then propagates along the longitudinal tow (Fig. 10a). Similarly, matrix cracks in directions oriented from 30 to 60°, or parallel, to the loading axis, are deflected and propagate along the longitudinal tows and around and through the transverse tows (Fig. 10b and c). Shear cracks, oriented from 30° to 60° to the loading axis, can allow contraction of the compressive tested specimens. Finally, the presence, in the fracture area, of a deleterious deformation and damage mechanism, such as a macroscopic shear band oriented at $\approx 45^{\circ}$ to the loading axis, explains the localization of failure under compressive loading (Fig. 10d). Such observations can be correlated with AE results, the more intense events probably corresponding to the nucleation of shear cracks, finally leading to delamination, to the formation of shear bands and, finally, to the composite failure. Such AE observations thus confirm the difference in nature and in chronology of the damage mechanisms occurring during tensile or compressive loadings to failure.

3.4. Difference between tension and compression damage mechanisms

The initiation of damage, leading to failure under compressive loading, *i.e.* shear cracks inclined at $\approx 45^{\circ}$ to the loading axis, leading to the formation of detrimental shear bands is thus completely different from the formation of transverse cracks leading to failure under tensile loading. In fact, two factors can have a major influence on the damage mechanisms leading to composite failure under tensile or compressive loadings: the stress concentrations resulting from the presence of macropores and the undulation of the longitudinal and transverse tows.

The role of macropores in the nucleation of cracks is completely different, when the composite is subjected to either tensile or compressive loading. The difference between these two situations is clearly evidenced when considering the macropore as a cylindrical hole in a plate (Fig. 11). Stress concentrations (circumferential stress component) appear on the edge of the hole [21]. Under tensile loading, the high stress concentration (a factor of 3), in a direction perpendicular to the loading axis, leads to the nucleation of cracks perpendicular to the loading axis (Fig. 11a). These cracks are thus often parallel to the sintering shrinkage cracks. The resulting matrix multicracking and the deflection and propagation of these cracks, along the longitudinal tows and around and through the transverse tows, play a major role in the elongation of the composite under tensile loading. Under compressive loading, the stress concentration factor is lower, but opposite in sign (−1 instead of 3) and in a direction parallel to the loading axis, it can thus lead to the nucleation of cracks parallel to the loading axis (Fig. 11c). Such cracks can

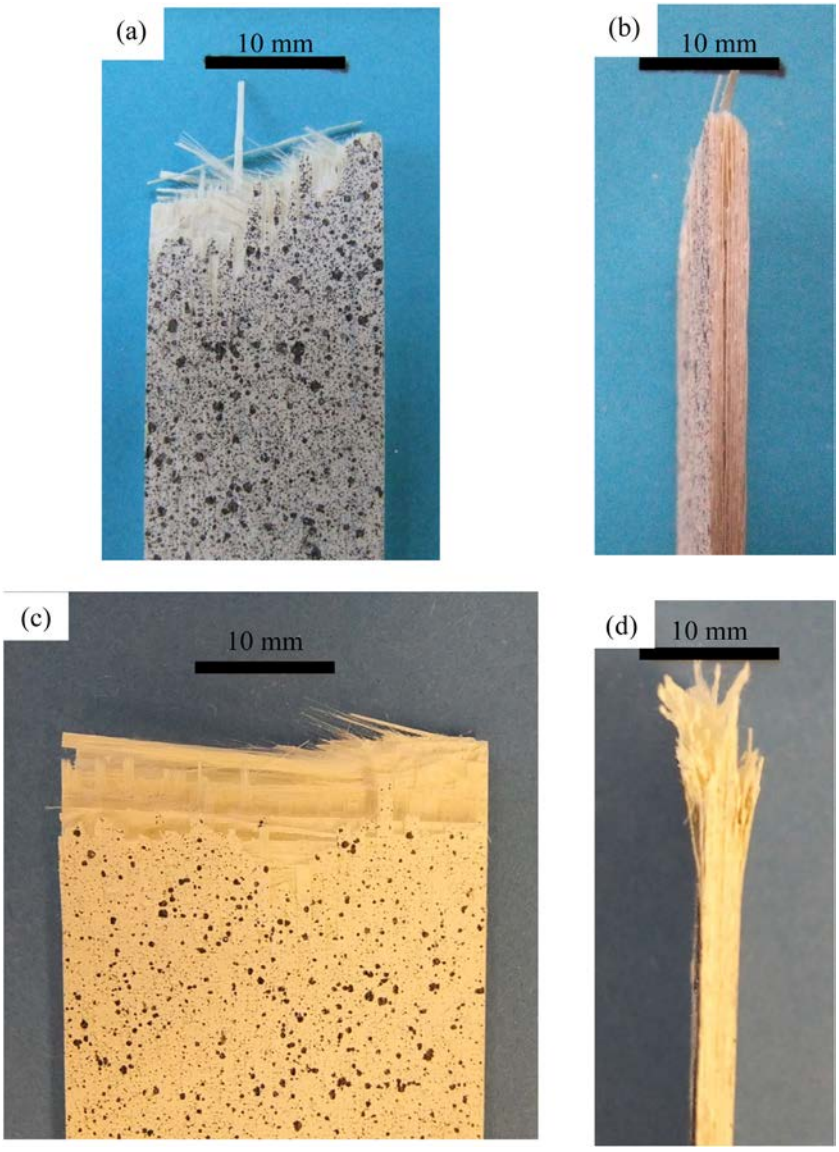

Fig. 7. Fracture surfaces of Nextel^{TM}610/alumina composites after tensile (a and b), and compressive (c and d) testing to failure. (a and c) Front views. (b and d) Side views.

propagate along the longitudinal tows and lead to delamination. Consequently, the role of matrix macropores is markedly different under either tensile or compressive loadings, since it leads to matrix multicracking in the first case and to delamination in the second case (Fig. 11b and d).

Regarding the role of the undulation of the tows in the woven fabric, SEM observations of Nextel^{TM}610/alumina composites have evidenced the specific role of such an undulation in the deformation mechanisms leading to failure under either longitudinal tensile or compressive loading (Fig. 12). Under tensile loading, the observation of transverse sections clearly demonstrates that the undulation amplitude of the transverse tows, increased through straightening of the longitudinal tows, leads to debonding of the longitudinal tows from the matrix and to nucleation and propagation of cracks in the longitudinal tows (Fig. 12a). It can also lead to debonding of one of two adjacent longitudinal tows (Fig. 12b). Thus, due to the longitudinal extension of the specimen under tensile loading, the increased undulation amplitude of the transverse tows through straightening of the longitudinal tows, contributes to interply debonding and thus to delamination.

Understanding the behaviour under compressive loading of the composite necessitates a comparison with unidirectional composites. In this case, the fibres are prevented from buckling (instability) for two reasons: first of all, some of them are straight, which requires attaining a critical load for buckling, and, secondly, they are firmly held in the matrix. However, when the unidirectional composite is subjected to a heavy compressive loading, the necessity to shorten the specimen finally leads to fibre buckling and kinking, thus resulting in the formation of kink-bands [22]. On the contrary, in the case of a woven composite, the fibres are already undulated. In a weak matrix CMC, the matrix can only impede further undulation of the longitudinal tows at the very beginning of the test, before marked damage of the matrix and of the transverse tows. As soon as the matrix and the transverse tows are sufficiently damaged to allow longitudinal contraction under the effect of the compressive loading, especially through matrix shear cracks oriented at approximately 45° to the loading direction (Fig. 10b and c), the undulation amplitude of the longitudinal tows is increased through compressive loading. This increase in the undulation amplitude of the longitudinal tows leads to nucleation and propagation of cracks around and through the transverse tows, to local debonding of the

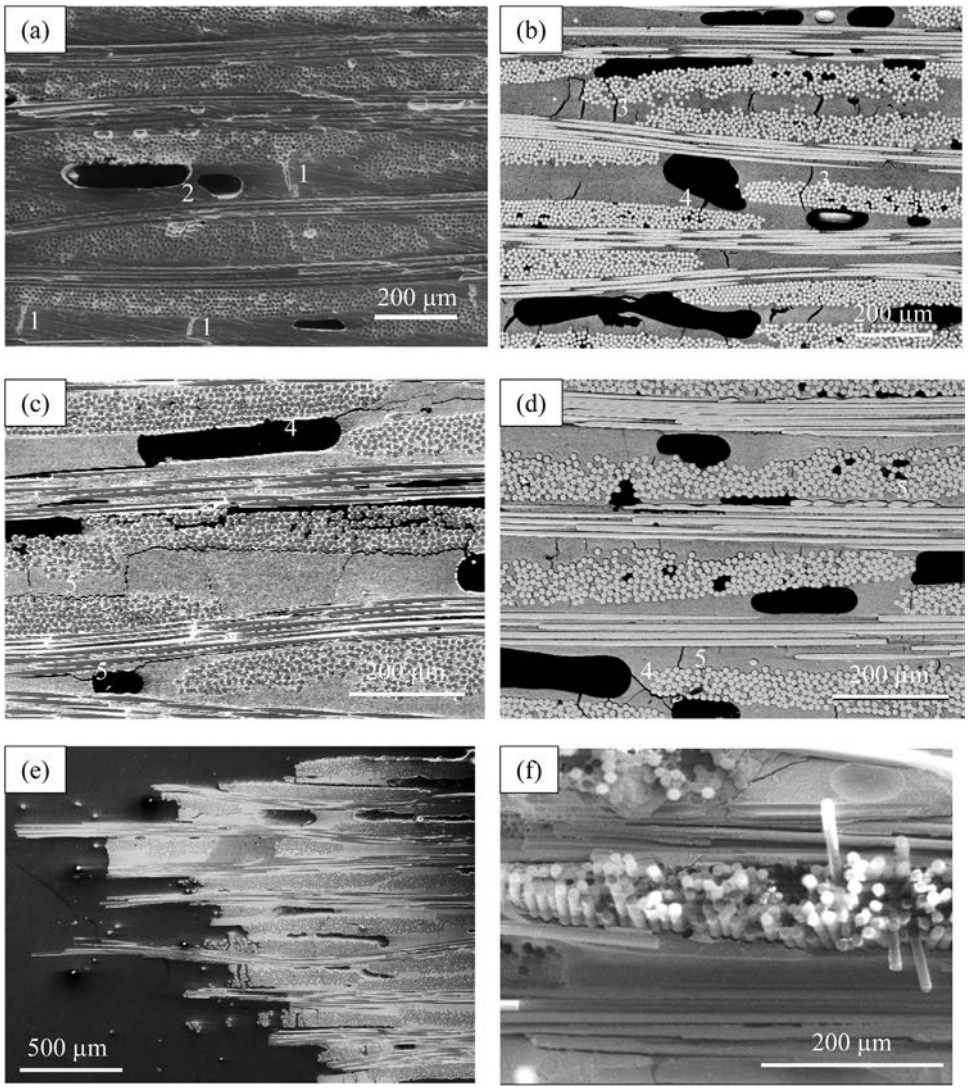

Fig. 8. SEM observations of longitudinal sections (a, b, c, d and e) and fracture surface (f) of a NextelTM610/alumina composite loaded in the fibre (weft) direction under different tensile loadings and tested to failure. (a) 165 MPa: inter-tow matrix cracks perpendicular to the loading axis (1) and absence of crack nucleation on the macropores (2). (b) 220 MPa: inter-tow matrix cracks perpendicular to the loading axis which propagate across the transverse tows (3). Nucleation and propagation of cracks on the macropores (4). (c and d) Failed specimen, matrix cracks, perpendicular to the plies, deflected at the fibre/matrix interface (5), crack initiation at macropores (4). (e) Tows and fibres pull-out. (f) Fibre/matrix debonding within the longitudinal tow.

longitudinal tows from the matrix or to compression of these tows against the matrix (Fig. 12c), thus contributing to the out-of-plane extension of the specimen and, finally, to delamination.

Consequently, for both tensile and compressive loadings, the resulting increase in the undulation amplitude of the transverse or, respectively, longitudinal tows of the woven fabric, leads to the same damage mechanism: delamination between the plies of the composite plate.

4. Concluding remarks

The microstructure of Nextel^{TM}610/alumina composite was investigated in order to assess its influence on the mechanical behaviour of the composite and to identify the damage mechanisms leading to failure under tensile and compressive loadings.

The as-processed material is pre-damaged, showing sintering shrinkage matrix microcracks and porosity. Three types of pores can be differentiated: matrix nanopores (< 0.1 µm), micropores, including matrix microcraks (< 10 µm) and inter- and intraply macropores (> 10 µm).

Mechanical properties were measured under tensile and compressive loadings and three-point bending tests (260 MPa and −291 MPa ultimate strengths under tensile and compressive loadings, respectively, and 20 MPa for ILSS). Young's moduli, graphically determined, were 161 ± 11 GPa under compressive loading and 134 ± 19 GPa under tensile loading. Then, damage mechanisms were studied using microstructural data, *in situ* tensile tests in SEM and AE data. The damage thresholds were graphically estimated and reach 48 ± 8 MPa, 0.04 ± 0.01 % and -123 ± 31 MPa, -0.08 ± 0.02 % under tensile and compressive loadings, respectively. They correspond to the initiation of the first damage, essentially matrix crack nucleation. Under compressive loading, closure of the matrix sintering shrinkage cracks and residual tensile stresses in the sintered matrix delay the initiation of specific damage mechanisms compared to tensile loading.

Although different under tensile and compressive loadings, damage mechanisms lead to delamination. Under tensile loading, deflection of the transverse cracks along the longitudinal tows, as well as an increase in the undulation of the transverse tows through straightening of the longitudinal tows, lead to delamina-

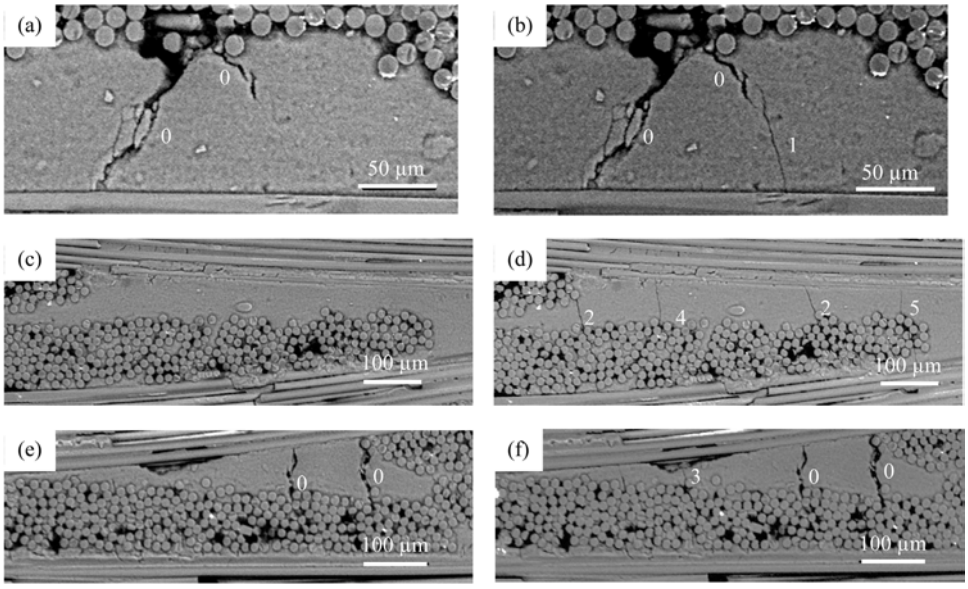

Fig. 9. *In situ* tensile testing (SEM) of Nextel™610/alumina composite. (a, c and e) As-processed material. (b) the same area as (a) under 63 MPa loading, (d and f) the same areas as (c and e) under 287 MPa loading. (b) Matrix crack formation at 63 MPa, (d) matrix cracks initiations in a transverse tow and propagation in the matrix. (f) A crack, nucleated in a transverse tow, falling into a macropore. (Chronology of crack initiations: 0, sintering shrinkage cracks; 1, crack initiation under 63 MPa; 2, under 112 MPa; 3, under 128 MPa; 4, under 192 MPa and 5, under 223 MPa loading).

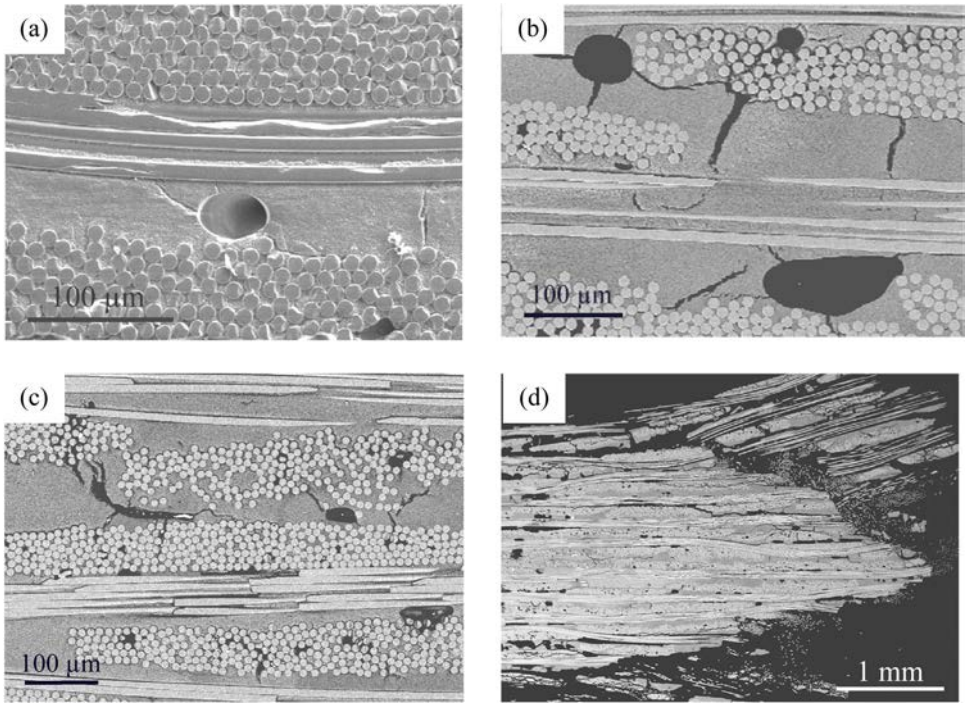

Fig. 10. SEM observations of longitudinal sections of Nextel™610/alumina composites compression tested to failure: (a) crack nucleation at the edge of a macropore in a direction parallel to the loading axis, deflection of this crack in a direction oriented at ≈ 45° to the loading axis and along the longitudinal tow, (b and c) matrix cracks in directions oriented from 30 to 60°, or parallel, to the loading axis, deflection of these cracks along the longitudinal and around and through the transverse tows, (d) failure localization on a macroscopic shear band.

tion. Under compressive loading, propagation of the longitudinal cracks, as well as an increase in the undulation of the longitudinal tows, lead to delamination. However, despite these delamination mechanisms which essentially result from the woven nature of the reinforcement and from the presence of macropores, the 2D Nextel™610/alumina composite exhibits rather high mechanical properties compared to the results published in the literature on similar materials. Macropores, essentially due to the manufacturing process, participate to crack initiation and propagation, but they can also stop short local cracks nucleated in neighbouring transverse tows, thus acting as crack sinks. Hence, even if the number of macropores should be reduced, they do not have to be totally suppressed. Only interply macropores, which lead to delamination under compressive loading, have to be eliminated. In conclusion, the mechanical properties are strongly related to the type of porosity and to the fibre volume fraction. In the present case, the obtained

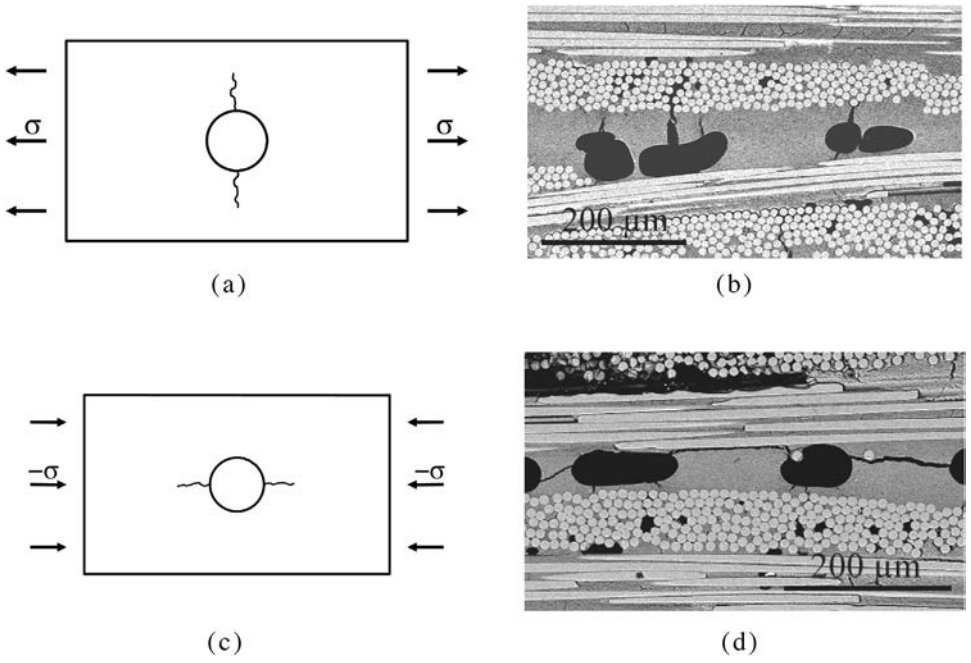

Fig. 11. Difference in the role of macropores (assimilated to cylindrical holes in a plate) in the initiation of cracks in the matrix of the composite subjected to either tensile (a and b) or compressive (c and d) loadings: crack nucleation resulting from stress concentration factors of 3 (a) and −1 (c) and cracks observed in specimens loaded to failure in tension (b) or compression (d).

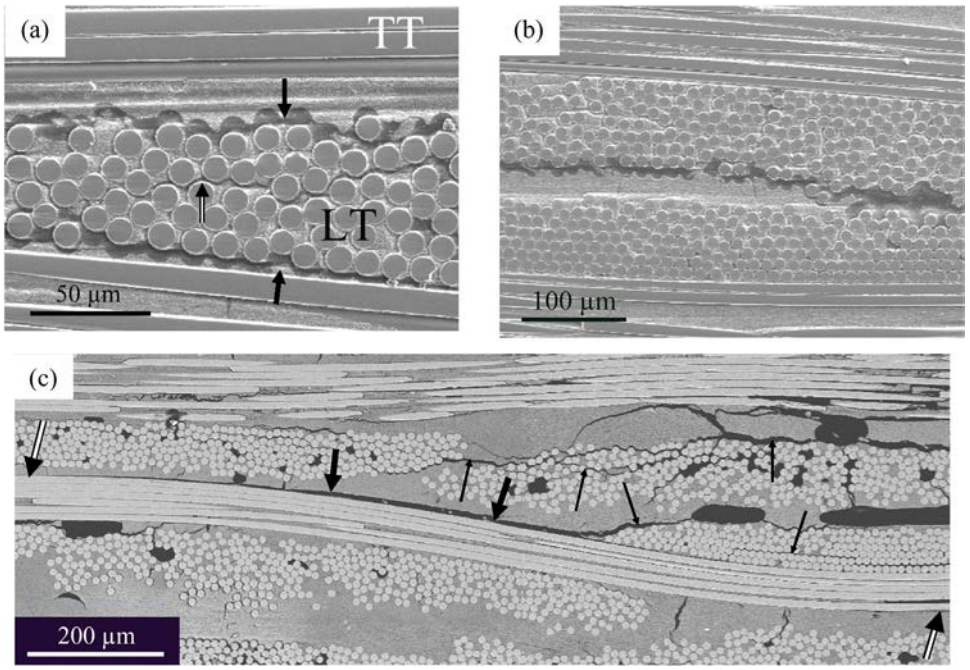

Fig. 12. SEM observations of Nextel™610/alumina composites evidencing the role of the undulation of the tows in the deformation mechanisms leading to failure under longitudinal tensile (transverse sections in (a) and (b)) and compressive (longitudinal section in (c)) loadings: (a) the undulation amplitude of the transverse tows (TT), increased through straightening of the longitudinal tows (LT) under tensile loading, leads to debonding of the longitudinal tows from the matrix (black arrows) and nucleation and propagation of cracks in the longitudinal tows (split arrow), or, (b) debonding of one of two adjacent longitudinal tows. (c) The undulation amplitude of the longitudinal tows, increased through compressive loading, leads to nucleation and propagation of cracks around and through the transverse tows (thin black arrows), to debonding of the longitudinal tows from the matrix (large black arrows) and to compression of these tows against the matrix (split arrows).

results clearly confirm that quite a good compromise has been reached between porosity, its spatial distribution and the mechanical properties.

Acknowledgements

The collaboration with *Herakles* is gratefully acknowledged. This work was supported under the PRC Composites, a French research project funded by *DGAC*, involving *Safran Group*, *ONERA* and *CNRS*.

The authors would like to thank *Safran Composites* for conducting X-ray tomography on their specimens. The authors are thankful to Dr. F. Laurin (ONERA, DMSC) for developing the method of analysis of X-ray tomography data used in this study. The authors would like to thank M.-H. Ritti (ONERA, DMSC) for her help in materials processing, F. Passilly and Dr. J.-M. Roche (ONERA DMSC) for NDT inspections and more particularly, A. Mavel (ONERA, DMSC) for the mechanical testing of the specimens. The authors are also grateful to D. Boivin and N. Horezan (ONERA, DMSM) who co-developed and conducted SEM *in situ* testing, and to M. Bejet (ONERA, DMSC) who designed specific jaws adapted to the *in situ* tensile testing of parallelepipedic shaped composite specimens.

Appendix A.

In the elastic region, considering firstly the 2D woven composite (total fibre volume fraction V_f) as a UD composite having a volume fraction, V_{fL}, of longitudinal fibres, a very rough estimate of the longitudinal Young's modulus, E_{cL}, of this composite, would be given by the rule of mixtures (ROM) in the longitudinal direction (Voigt):

$$E_{cL} = (1 - V_{fL} - V_{Mp+\mu p})E_m + V_{fL}E_{fL} \quad (A.1)$$

where E_m is the Young's modulus of the matrix (neglecting the transverse tows), E_{fL} the longitudinal Young's modulus of the fibres and $V_{Mp+\mu p}$ the volume fraction of both macropores and micropores, the nanopores being included in the matrix volume fraction.

The transverse tows can be taken into account by considering the matrix as a transverse UD composite reinforced by the transverse tows. The fibre volume fraction, V_{fmT}, in this "composite matrix" is given by

$$V_{fmT} = V_{fT}/(V_m + V_{fT})$$

where V_{fT} is the volume fraction of transverse fibres.

In the present case

$$V_{fL} = V_{fT} = 0.5\,V_f$$

A rough estimate of the transverse Young's modulus of the "composite matrix", E_{cmT}, is then given by the rule of mixtures in the transverse direction (Reuss)

$$1/E_{cmT} = (1-V_{fmT})/E_m + V_{fmT}/E_{fT}$$

where E_{fT} is the transverse Young's modulus of the fibres, in the present case

$$E_{fL} = E_{fT} = E_f$$

Finally, taking the transverse tows into account, the corrected longitudinal Young's modulus of the 2D composite, E_{cL}^*, is given by

$$E_{cL}^* = (1\text{-}V_{fL} - V_{Mp+\mu p})E_m^* + V_{fL}E_{fL} \quad (A.2)$$

where $E_m^* = E_{cmT}$.

For the investigated 2D N610^{TM}/alumina composite, $E_{cL}^* = 164$ GPa.

Appendix B.

The composite being subjected to a longitudinal applied stress, σ_z, the resulting longitudinal stress component in the matrix, σ_{mz}, can be easily determined (theory of linear elasticity). The longitudinal tows exhibiting a flat elliptical cross-section, the composite can thus be modeled as a composite plate consisting of two long and perfectly bonded parallelepipeds subjected to a longitudinal loading, σ_z. The first plate is supposed to have the mechanical properties of the fibres and a rectangular cross-section proportional to the volume fraction of the longitudinal fibre tows, V_{fL}, *i.e.* an (E_{fL}, V_{fL}) "fibre" plate. The second plate consists in a matrix block having the mechanical properties of the nanoporous matrix and a rectangular cross-section proportional to the matrix volume fraction ($1 - V_{fL} - V_{Mp+\mu p}$), *i.e.* an ($E_m$, $1 - V_{fL} - V_{Mp+\mu p}$) "matrix" plate, where $V_{Mp+\mu p}$ is the volume fraction of both macropores and micropores.

If the composite plate is subjected to a longitudinal loading, σ_z, then

$$(B.1)\ \sigma_z = V_{fL}\sigma_{fz} + (1 - V_{fL} - V_{Mp+\mu p})\sigma_{mz}$$

where σ_{fz} and σ_{mz} are the longitudinal stress components in the "fibre" plate and in the "matrix" plate, respectively.

If the condition of generalized plane strain in a transverse section of the composite plate is assumed, then

$$(B.2)\ \varepsilon_z = C^{st} = \varepsilon_{fz} = \varepsilon_{mz}$$

where ε_{fz}, ε_{mz} and ε_z are the longitudinal strain components in the "fibre" plate, the "matrix" plate and the composite plate, respectively.

Then

$$\sigma_{fz} = E_f\varepsilon_z \quad (B.3)$$

$$(B.4)\ \sigma_{mz} = E_m\varepsilon_z$$

Combining the relations (B.1), (B.3) and (B.4) yields

$$\sigma_{mz} = \frac{E_m}{V_{fL}E_f + (1\text{-}V_{fL}\text{-}V_{Mp+\mu p})E_m}\sigma_z \quad (B.5)$$

In the present case

$$\sigma_{mz} \approx 0.56\sigma_z$$

References

[1] C.G. Levi, J.Y. Yang, B.J. Dalgleish, F.W. Zok, A.G. Evans, Processing and performance of an all-oxide ceramic composite, J. Am. Ceram. Soc. 81 (1998) 2077–2086.
[2] P.R. Jackson, M.B. Ruggles-Wrenn, S.S. Baek, K.A. Keller, Compressive creep behavior of an oxide–oxide ceramic composite with monazite fiber coating at elevated temperatures, Mater. Sci. Eng. A 454–455 (2007) 590–601.
[3] M.B. Ruggles-Wrenn, A.T. Radzicki, S.S. Baek, K.A. Keller, Effect of loading rate on the monotonic tensile behavior and tensile strength of an oxide–oxide ceramic composite at 1200 °C, Mater. Sci. Eng. A 492 (2008) 88–94.
[4] M.B. Ruggles-Wrenn, N.R. Szymczak, Effects of steam environment on compressive creep behavior of N720/alumina ceramic composite at 1200 °C, Composites A 39 (2008) 1829–1837.
[5] M.B. Ruggles-Wrenn, S. Mall, C.A. Eber, L.B. Harlan, Effects of steam environment on high-temperature mechanical behavior of Nextel^{TM}720/alumina (N720/A) continuous fiber ceramic composite, Composites A 37 (2006) 2029–2040.
[6] M. Parlier, M.H. Ritti, State of the art and perspectives for oxide/oxide composites, Aerosp. Sci. Technnol. 7 (2003) 211–221.
[7] P.E. Cantonwine, Strength of thermally exposed alumina fibers. Part II Bundle behaviour, J. Mater. Sci. 38 (2003) 471–480.
[8] F.W. Zok, C.G. Levi, Mechanical properties of porous-matrix ceramic composites, Adv. Eng. Mater. 3 (2001) 15–23.
[9] D. Koch, K. Tushtev, G. Grathwohl, Ceramic fiber composites: experimental analysis and modeling of mechanical properties, Comp. Sci. Technol. 68 (2008) 1165–1172.
[10] M.G. Holmquist, F.F. Lange, Processing and properties of a porous oxide matrix composite reinforced with continuous oxide fibers, J. Am. Ceram. Soc. 86 (2003) 1733–1740.
[11] M.A. Mattoni, J.Y. Yang, C.G. Levi, F.W. Zok, Effects of matrix porosity on the mechanical properties of a porous-matrix, all-oxide ceramic composite, J. Am. Ceram. Soc. 84 (2001) 2594–2602.
[12] D.M. Wilson, L.R. Visser, High performance oxide fibers for metal and ceramic composites, Composites A 32 (2001) 1143–1153.
[13] R.J. Kerans, R.S. Hay, T.A. Parthasarathy, Structural ceramic composites, Curr. Opin.Solid State Mater. Sci. 4 (1999) 445–451.
[14] M. Parlier, M.H. Ritti, A. Jankowiak, Potential and perspectives for oxide/oxide composites, J. Aerosp. Lab. (2011) AL3–AL09.
[15] C. Ben Ramdane, Etude et modélisation du comportement mécanique de CMC oxyde/oxyde, Ph.D dissertation, Université de Bordeaux, 2014 (in french).
[16] R.A. Simon, Progress in processing and performance of porous-matrix oxide–oxide composites, Int. J. Appl. Ceram. Technol. 2 (2) (2005) 141–149.

[17] M.B. Ruggles-Wrenn, S.S. Musil, S. Mall, K.A. Keller, Creep behavior of Nextel™610/monazite/alumina composite at elevated temperatures, Comp. Sci. Technnol. 66 (2006) 2089–2099.
[18] L.P. Zawada, R.S. Hay, S.S. Lee, J. Staehler, Characterization and high-temperature mechanical behavior of an oxide/oxide composite, J. Am. Ceram. Soc. 86 (6) (2003) 981–990.
[19] R.A. Jurf, S.C. Butner, Advances in oxide–oxide CMC, J. Eng. Gas Turbines Power 122 (2000) 202–205.
[20] V. Kostopoulos, T.H. Loutas, A. Kontsos, G. Sotiriadis, Y.Z. Pappas, On the identification of the failure mechanisms in oxide/oxide composites using acoustic emission, Nondestruct. Test. Eval. Int. 36 (2003) 571–580.
[21] S.P. Timoshenko, J.N. Goodier, Theory of Elasticity, 3rd ed., McGraw-Hill, New-York, 1970, pp. 90–92.
[22] J. Lankford, Compressive failure of fibre-reinforced composites: buckling, kinking, and the role of the interphase, J. Mater. Sci. 30 (1995) 4343–4348.